ROYAL SOCIETY
OF CHEMISTRY

PAPER

View Article Online
View Journal | View Issue

Bulk boron doping and surface carbon coating enabling fast-charging and stable Si anodes: from thin film to thick Si electrodes†

Xiang Han,[ab] Ziqi Zhang,[b] Huixin Chen, [c] Linshan Luo,[b] Qiaobao Zhang, [e] Jizhang Chen,*[a] Songyan Chen [*b] and Yong Yang [*d]

To address the issues of the particle fracture and loss of electrical connectivity of high capacity silicon anodes, herein, we propose a novel strategy that combines surface carbon coating and bulk boron doping. Heavily boron doped polycrystalline photovoltaic Si particles are used as starting materials. The bulk boron doping is demonstrated to enhance both electron transportation and lithium-ion diffusion, which contributes to superior high-rate performance. Taking advantage of the fast kinetics and stable interphase with the electrolyte, the carbon coated boron doped Si electrode exhibits higher capacity retention. For example, the capacity retentions are 668 mA h g^{-1}, 293 mA h g^{-1} and 79 mA h g^{-1} at a high rate of 0.5C (1C = 4000 mA g^{-1}) after 500 cycles for 3900 ppm, 120 ppm, and 10 ppm boron doped Si, respectively. In addition, an improved mass loading of 2.0 mg cm^{-2}, high areal capacity (3.9 mA h cm^{-2}) and high-volume capacity (2111 mA h cm^{-3}) are achieved. Our work opens a new horizon for designing stable high loading Si anodes, which is applicable for other alloy electrode materials.

Introduction

Lithium-ion batteries play an important role in the market of electric vehicles (EVs), due to their higher energy density and good cycling stability compared with aqueous batteries or supercapacitors.[1–5] To further improve the mileage and reduce the charging time, we should turn to new materials with high specific capacity and high rate performance. Among various anodes, silicon shows the highest theoretical specific capacity of ~3650 mA h g^{-1} ($Li_{15}Si_4$) at room temperature.[6–8] The practical application of Si anodes, especially at high rates, however, is hampered by their large volume change, low electrical conductivity and unstable solid electrolyte interphase (SEI).[9–11] Surface coating has been demonstrated to be an effective way to release the stress during volume expansion and thus help to improve the particle integrity. To date, lots of coating materials

including metals, ceramics, carbon, and MXenes have been evaluated.[12–16] Various approaches for the coating of Si nano-sized particles by ALD,[17] PVD,[18] and sol–gel[19] have been developed. Regardless of the improvement in electrochemical cycling stability and rate performance (with a conductive metal or carbon coating layer), there are still two remaining issues to be resolved: (1) the low intrinsic conductivity of bulk Si retards the transportation of electrons and lithium ions, especially for micrometer-sized particles, which are usually needed for high areal capacity or high loading electrodes; (2) the poor conductivity between active materials and the current collector after several cycles. The Si particles still fracture into small particles even with some coating materials, which causes the loss of electrical conductivity and electrochemical activity.

Very recently, some researchers focused on phosphorus[20,21] and sulfur doping,[22] giving us a concept that doping is an effective strategy to enhance the electrical conductivity and long-term durable cycling performance of Si anodes. Both phosphorus and sulfur doping are N-type doping, either from microelectronic Si or complex doping processes. In addition, P-type (boron doping) high purity Si wafers in microelectronics have also been evaluated.[23] A P-type Si material is normally used in the solar cell industry, during the sheet Si fabrication process, and tons of Si waste fragments are formed. The purity of this Si is not very high (4 N, 99.99%), and may contain B, Fe, Al, Ca, Ti, Ni and so on. The boron doping contents can be easily controlled during the crystallization and purification processes. Moreover, the starting materials and boron doping method described here are facile and cheap. However, the application of

[a]College of Materials Science and Engineering, Co-Innovation Center of Efficient Processing and Utilization of Forest Resources, Nanjing Forestry University, Nanjing 210037, China. E-mail: chenjizhang@njfu.edu.cn

[b]Department of Physics, Xiamen University, Xiamen 361005, China. E-mail: sychen@xmu.edu.cn

[c]Xiamen Institute of Rare Earth Materials, Haixi Institutes, Chinese Academy of Sciences, Xiamen 361021, China

[d]State Key Laboratory for Physical Chemistry of Solid Surfaces, Department of Chemistry, Xiamen University, Xiamen 361005, China. E-mail: yyang@xmu.edu.cn

[e]Department of Materials Science and Engineering, College of Materials, Xiamen University, Xiamen 361005, China

this kind of boron doped Si in lithium-ion batteries has not been reported.

In this paper, a boron doped a-Si thin film is used to evaluate the effects of boron doping on electrochemical performance. Due to the electrical conductivity improvement of boron-doped Si, the rate performance significantly enhances. In addition, the boron doped thin film Si electrode shows a typical capacity increasement after around 100 cycles, which is attributed to the improvement of inter-conductivity and a recharging effect.

To improve the SEI stability and to synthesis thick Si in a scalable method, we extend the starting materials to poly-crystalline Si particles (120 mesh) in the solar cell industry. After carbon coating, the Si electrode with 3900 ppm boron doping shows a lithium diffusion coefficient 7.6 times higher than that of 10 ppm Si. Taking advantages of fast lithium ions/electrons transportation and the SEI stability, high areal capacity achieved. The carbon coated boron doped Si electrode exhibits high areal capacity (3.9 mA h cm^{-2}) and high-volume capacity (2111 mA h cm^{-3}). We call for bulk doping and surface passivating engineering to achieve high loading thick Si anodes, which will meet the commercial criterion (>3 mA h cm^{-2}).

Results and discussion

Thin-film boron doped a-Si film

Fig. 1(a) shows the schematic of boron doped a-Si deposited on a copper film by a radio frequency sputtering method. By comparison, Si wafers (boron doping) with conductivities of 5–7 mΩ cm and 1–10 Ω cm were selected as targets. After 1 h sputtering (Fig. 1(b)), the boron doped a-Si uniformly coated on the surface of the rough copper film. The thickness of a-Si was

measured to be 250 nm on a clean Si wafer. The initial charge and discharge curves of a-Si electrodes are shown in Fig. 1(c), and two typical plateaus of a-Si at 0.2 V and 0.1 V are observed.[24] The test voltage window is 0.005–2.5 V, and 1C = 4000 mA g^{-1}. The initial capacity of 5–7 mΩ cm and 1–10 Ω cm are 2259 and 2102 mA h g^{-1} at 0.25C, respectively. The initial coulombic efficiencies of 5–7 mΩ cm and 1–10 Ω cm are 78.5% and 74.4%, respectively. The a-Si thin film electrode with heavy boron

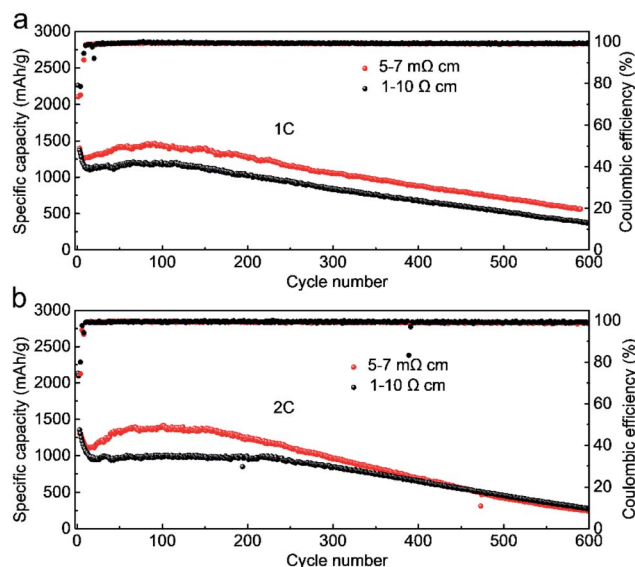Fig. 2 Long-term cycling performance of boron doped a-Si thin film anodes at (a) 1C and (b) 2C. 1C = 4000 mA g^{-1}; the voltage window is 0.005–2.5 V.
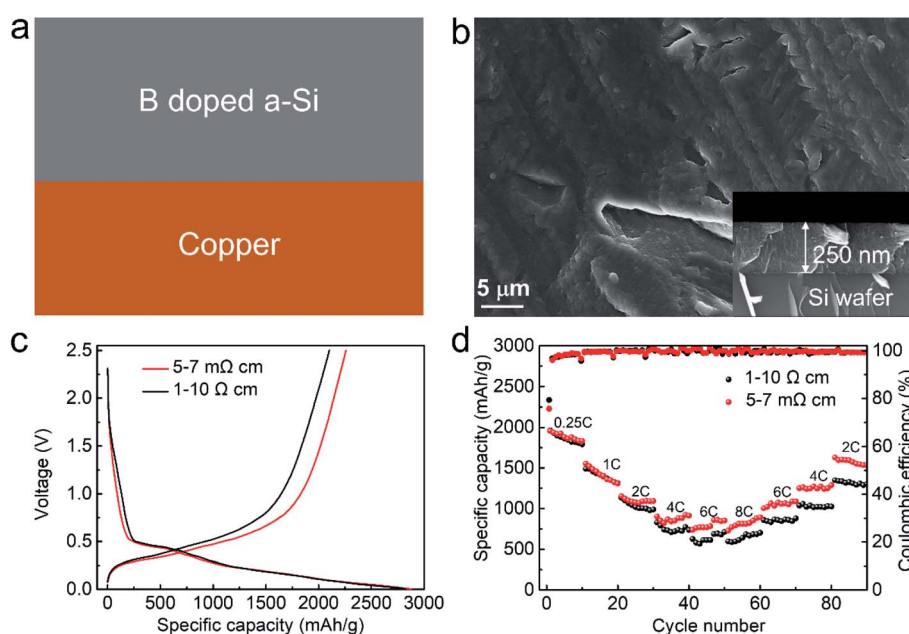

Fig. 1 (a) Schematic illustration of the boron doped a-Si directly deposited on a copper film by RF-sputtering. (b) Surface and cross-sectional SEM images of the sputtered a-Si, and the inset shows the a-Si on Si wafer. (c) The initial charge–discharge profiles of boron doped a-Si anodes with different boron doping amounts at 0.25C between 0.005 and 2.5 V. (d) The rate performance of boron doped a-Si anodes with different boron doping amounts (1C = 4000 mA g^{-1}).

This journal is © The Royal Society of Chemistry 2021

J. Mater. Chem. A, 2021, **9**, 3628–3636 | **3629**

doping exhibits higher capacity retention at a higher rate. For example, as shown in Fig. 1(d), the capacities of 5–7 mΩ cm and 1–10 Ω cm at 8C are 893 mA h g^{-1} (46%) and 702 mA h g^{-1} (36%), respectively.

To estimate the effect of boron doping on the long-term cycling stability, galvanostatic tests at 1C and 2C were carried out. As shown in Fig. 2(a), for the capacity of the a-Si anode with a conductivity of 5–7 mΩ cm fades quickly to 1302 mA h g^{-1} during the initial 20 cycles. After that, the capacity slowly increases to 1429 mA h g^{-1} in the 100th cycle and the capacity retention is 563 mA h g^{-1} after 590 cycles. By contrast, no obvious capacity increasement after 20 cycles is observed for the a-Si anode with a 1–10 Ω cm conductivity and the capacity retention after 600 cycles is only 367 mA h g^{-1}. For boron-doped Si, there is a period around 100 cycles during which the capacity

increases slightly, which contributes to the following two mechanisms. (1) The recharging process, because more lithium caught in the first cycle as the irreversible capacity, the storaged capacity could recharge the cell during lateral cycles. For example, the initial coulombic efficiency of B10 is 78.5–80.5% and that of B3900 is 74.4–75.8% (Fig. 1(d), 2(a) and (b)). (2) The enhanced electrical conductivity, becasue the conductivity between the *in situ* formed nanoscale or porous Si is critical to remain the electrochemical activity. With this in mind, we conclude that the boron doping could improve capacity retention by electrically binding the porous Si/Li$_x$Si structure together during lithiation/delithiation. This hypothesis is further confirmed by the cycling performance at 2C, as shown in Fig. 2(b); a capacity increment is observed for the 5–7 mΩ cm a-Si anode; Both a-Si anodes with different conductivity show the
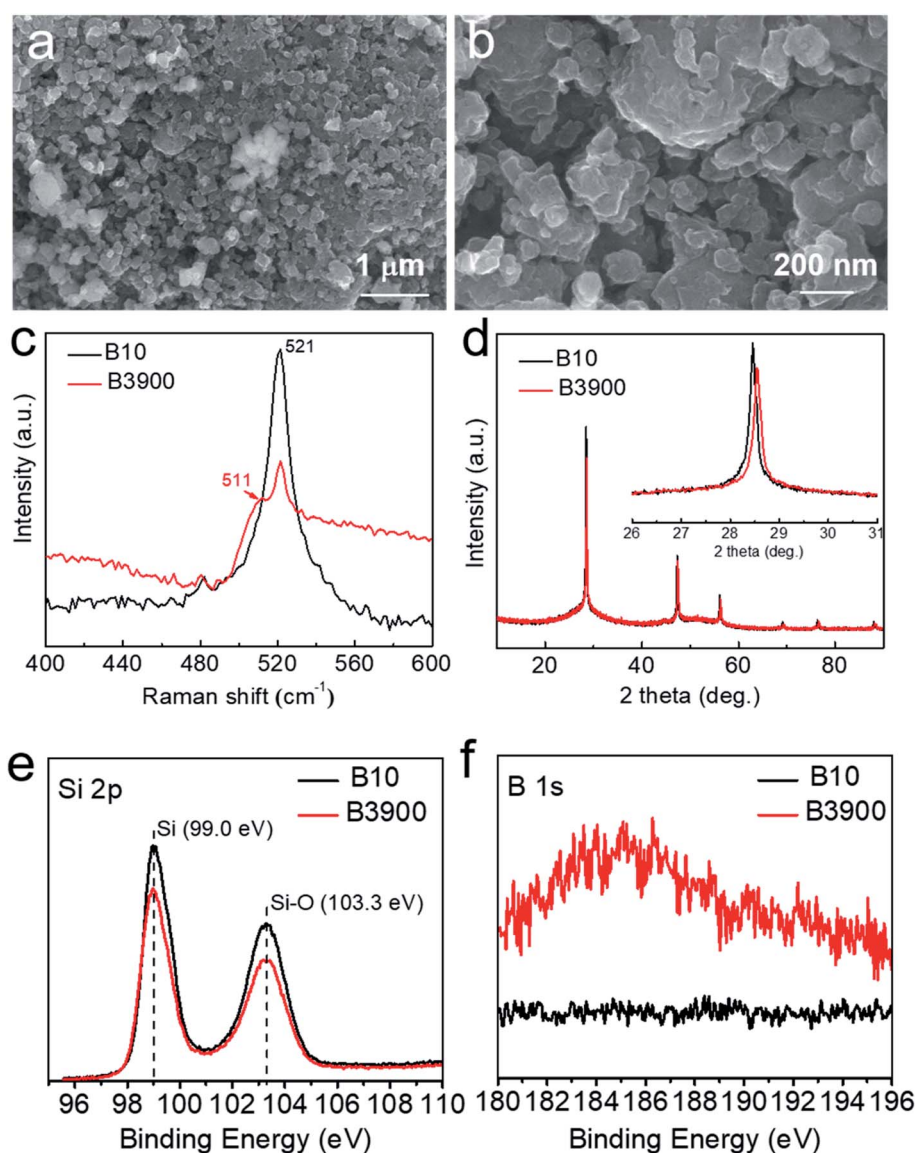

Fig. 3 (a) The SEM image of the as-synthesized boron doped Si particles. (b) A high magnification view in (a). (c) Raman spectra of the synthesized Si particles with different boron doping amounts. (d) X-ray diffraction patterns of the synthesized Si particles with 10 and 3900 ppm boron doping. XPS spectra of Si particles with 10 and 3900 ppm boron doping: (e) Si 2p and (f) B 1s.

3630 | *J. Mater. Chem. A*, 2021, **9**, 3628–3636

This journal is © The Royal Society of Chemistry 2021

same capacity retention of 250 mA h g^{-1} after 600 cycles. Without the protection of a surface coating layer, the boron doped a-Si materials continuous react with the liquid electrolyte and form a thick SEI layer, eventually losing capacity.

Thick Si electrodes based on polycrystalline boron-doped photovoltaic Si

To synthesis boron doped Si in a scalable method and to passivate its surface, with microscale polycrystalline Si particles (120 mesh) as starting materials, we directly fabricate boron doped nano-Si particles by a simple ball milling method. The morphology of the as-synthesized boron doped nano-Si particles (3900 ppm boron doping namely B3900) is shown in Fig. 3(a), and the particles show a wide size range of 100 nm to 2 μm based on laser analysis (Fig. S1†). In a high magnification view (Fig. 3(b)), the sharp and smooth edges of pristine Si turn into irregular particles with some small pores. As shown in Fig. 3(c), Raman spectroscopy was used to characterize the vibration mode of the synthesized boron doped nano-particles. For the B10 sample, a sharp peak at 521 cm^{-1} is attributed to the vibration of the crystalline Si–Si bond.[25] However, for the B3900 sample, besides a broad peak at 521 cm^{-1}, a new shoulder peak at 511 cm^{-1} is observed. Considering that the Raman peak of amorphous Si is located at 480 cm^{-1},[25] the small red shift from 521 to 511 cm^{-1} of the Si material with boron doping is due to the lattice deformation caused by the stress in the surrounding Si atomic network by B doping.[23] The X-ray diffraction (XRD) patterns of both the as-synthesized samples show typically diffraction patterns of cubic structured Si, which is shown in Fig. 3(d). The two-theta degree of the B3900 sample is higher than that of the B10 sample, implying a smaller inter-plane space. Because the radius of the boron atom is smaller than that of the Si atom, boron doping induces a smaller inter-plane spacing. In X-ray photoelectron spectroscopy (XPS) spectra, the Si 2p spectrum of both B10 and B3900 shows two peaks at 99.0 eV and 103.3 eV (Fig. 3(e)), corresponding to the

Si–Si and Si–O bonds, respectively.[26] However, for B 1s spectra, a broad peak between 184 and 188 eV was detected for the B3900 sample, while no peak was observed for the B10 sample (Fig. 3(f)). Based on the XPS results, the Si, boron and oxygen contents of the B3900 surface are 43.88%, 5.29%, and 50.83%, respectively. The XPS results further confirm the boron doped nature of the as-synthesized nano-Si particles.

A carbon coated and boron doped Si electrode was then fabricated to further improve cycling stability. The boron doped Si particles are uniformly dispersed in the carbon matrix (Fig. 4(a)). The amorphous carbon serves as both a binder and a coating layer. The surface carbon layer is observed in Fig. 4(b). The Si core shows polycrystalline nature, which is further confirmed by the electron diffraction patterns (Fig. 4(c) and (d)). To further analysis the elemental distribution of carbon coated boron doped nano-Si particles, a dark filed TEM image of a single particle and the corresponding EDS mapping were obtained (Fig. 4(e)). A uniform carbon signal was observed on the surface of the Si core, while the Si signal shows the same shape as the Si particle. As expected, a moderate boron signal was detected with the same shape of Si.

To evaluate the effects of boron doping and surface carbon coating on the electrochemical performance, the carbon coated boron doped Si was assembled in a coin cell with lithium metal as the counter electrode. The mass loading and specific capacity calculation is based on the total mass of Si and carbon, and the mass loading is between 1 and 2 mg cm^{-2}. The weight ratio of Si and amorphous carbon (including 4.4% N, 21.06% C and 1.08% H) was 73.46% and 26.54%, respectively. With a loading of 1 mg cm^{-2} at 0.1C (1C = 4000 mA g^{-1}) between 0.005 and 1.5 V, the B10 and B3900 anodes show initial capacities of 1845 and 2247 mA h g^{-1}, respectively (Fig. 5(b)). The capacity of both electrodes of B10 and B3900 fades quickly during the initial 20 cycles at 0.25C (Fig. 5(a)). After that, the electrodes show a stable cycling capacity of ~1200 mA h g^{-1}. However, the B10 electrode starts to degrade again after 100 cycles and the capacity
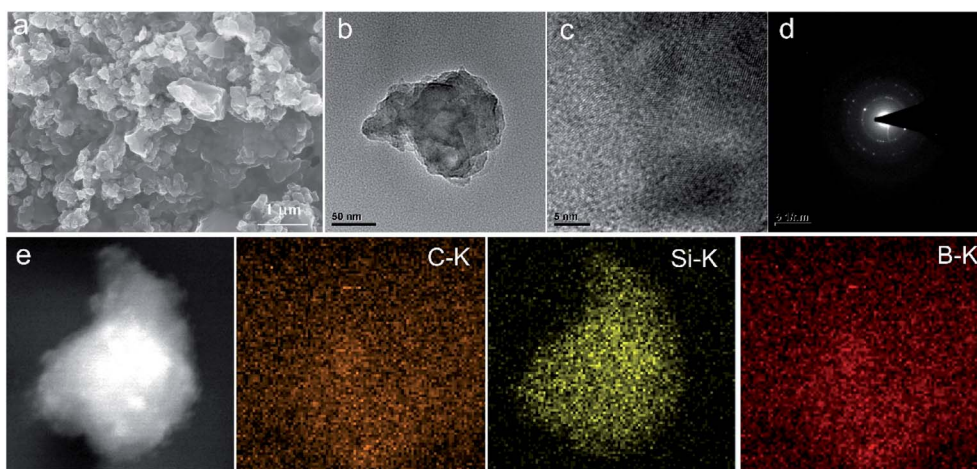

Fig. 4 (a) Surface SEM image of carbon coated boron doped Si particles. (b) TEM image of a separate carbon coated boron doped Si particle. (c) High-resolution TEM image in (b). (d) Electron diffraction patterns of picture (c). (e) Dark filed TEM image of a separate carbon coated boron doped Si particle and corresponding energy dispersive elemental mapping.

This journal is © The Royal Society of Chemistry 2021

J. Mater. Chem. A, 2021, **9**, 3628–3636 | **3631**

retention after 300 cycles is 93 mA h g^{-1}. By contrast, the B3900 electrode exhibits more stable cycling performance and the capacity retention after 500 cycles is 738 mA h g^{-1}. At a specific current of 0.4 A g^{-1}, the electrodes show the same cycling trend, and the B3900 electrode exhibits a higher capacity retention of 926 mA h g^{-1} *vs.* a capacity of 434 mA h g^{-1} of the B10 electrode after 300 cycles (Fig. S2†). For carbon coated Si electrodes, boron doping was also demonstrated to improve the cycling stability.

To test the kinetics of boron doped Si electrodes, impedance and CV curves were obtained. For the EIS data after 2 charge and discharge processes (Fig. 5(d)), both the two electrodes show two semicircles, corresponding to the SEI (high frequency) and charge transfer resistance (middle frequency). Typically, the equivalent circuit consists of SEI resistance (R_{se}) in series with the charge transfer part (charge transfer resistance, R_{ct} in parallel with the constant phase element, CPE), and in series

with the Warburg element (W) (Fig. 5(c)). Based on this model, the fitting curves are well consistent with the original data (Fig. 5(d)). The R_{ct} of B10 and B3900 is 13.3 and 7.4 Ω, respectively (Table 1 in the ESI†). It is well known that at least two electrochemical processes are related to charge transfer resistance: lithium ion redox and its transportation at the interphase.[27] In addition, the diffusion coefficient was calculated based on eqn (1) and (2)[19,21]

$$D_{Li^+} = \frac{R^2 T^2}{2A^2 n^4 F^4 C^2 \sigma^2} \tag{1}$$

$$Z_{re} = R_{se} + R_{ct} + \sigma \omega^{-0.5} \tag{2}$$

The diffusion coefficient (D_{Li^+}) of boron-doped anodes is calculated according to eqn (1), in which R, T, A, n, F and C are the gas constant, absolute temperature, surface area of the electrodes, the number of electrons, Faraday constant and
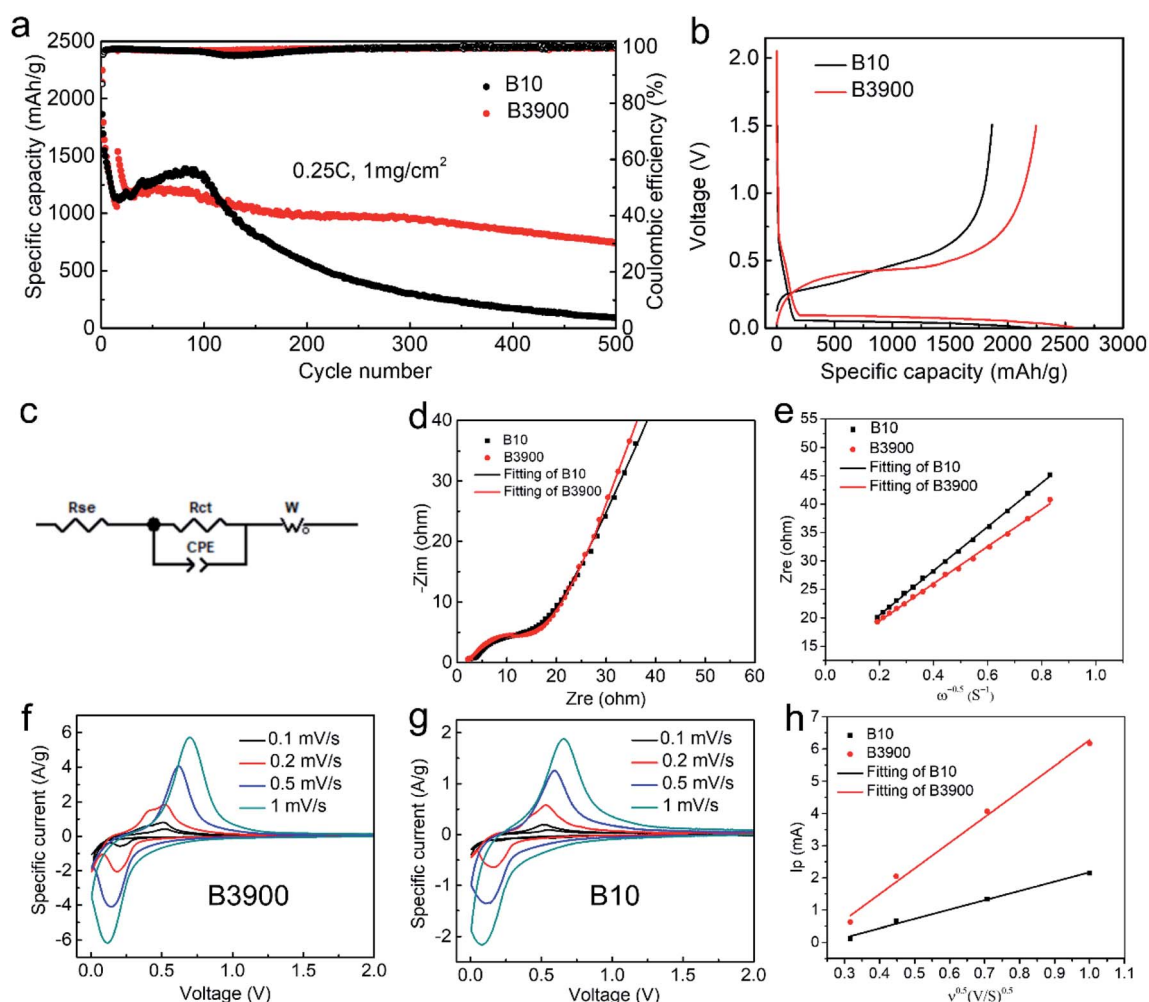

Fig. 5 (a) The cycling performance of carbon coated boron doped Si anodes with different boron doping amounts 10 and 3900 ppm, and the mass loading is around 1 mg cm^{-2}. (b) The initial capacity voltage profile of boron doped Si anodes at 0.25C (1C = 4000 mA g^{-1}), and the voltage range is 0.005–1.5 V. (c) The equivalent circuit of the cell containing B3900 and B10 electrodes. (d) Nyquist plots of carbon coated boron doped Si anodes with different boron doping amounts and corresponding fitting curves. (e) The relationship between Z_{re} and $\omega^{-0.5}$. (f) CV curves of the carbon coated boron doped Si (3900 ppm) anode from 0.1 to 1 mV s^{-1}. (g) CV curves of the carbon coated boron doped Si (10 ppm) anode from 0.1 to 1 mV s^{-1}. (h) The relationship of the peak current (I_p) and the square root of the scan rate ($v^{1/2}$).

lithium ion concentration, respectively; and σ is the Warburg factor. According to eqn (2), the values of σ are calculated from the fitted linear relationships between the real resistance (Z_{re}) and inverse square root of the angle frequency ($\omega^{-0.5}$), as shown in Fig. 5(e). The σ of B10 and B3900 is 38.78 and 32.69 $cm^2\ s^{-0.5}$, respectively. The calculated diffusion coefficient (D_{Li^+}) is 6.39×10^{-12} and $8.99 \times 10^{-12}\ cm^2\ s^{-1}$ (Table 1 in the ESI†), respectively.

Meanwhile, the lithium-ion diffusion coefficient of bulk Si significantly improved by boron doping. Fig. 5(f) and (g) show the CV curves at different scan rates. Normally the restraint process of the Si electrode is the lithium-ion diffusion, and the relationship between the peak current and the CV sweep rate is:[28]

$$I_p = 2.69 \times 10^5 n^{3/2} A D_{Li^+}^{1/2} C_{Li}^* v^{1/2} \qquad (3)$$

where I_p is the peak current, n represents the charge number of Li_xSi (for the first reduction peak, $n = 2.2$), A is the contact area (1 cm^2), D_{Li^+} is the diffusion coefficient, C_{Li}^* is the bulk concentration of lithium in the electrode (0.0753 mol cm^{-3} for Li_7Si_3), and v is the scan rate. The peak current shows a linear relationship with the square root of the scan rate (as shown in Fig. 5(h)). Based on the fitting results, the calculated diffusion coefficient of B10 and B3900 is 1.08×10^{-12} and 8.24×10^{-12} $cm^2\ s^{-1}$ (Table 2 in the ESI†), respectively. We demonstrate that the lithium transportation of heavily boron doped Si both in bulk or at the interface is improved. This is due to more vacancies formed after 3900 ppm boron doping into Si, and the effective carrier density improves and contributes to fast lithium-ion transportation.

The same cycling trend was also observed at a high rate of 0.5C. As shown in Fig. 6(a), the B3900 electrode shows a stable cycling performance after 20 cycles and retains 668 mA h g^{-1} after 500 cycles. For the B10 Si electrode, the specific capacity fades quickly after 120 cycles and it only retains a specific capacity of 79 mA h g^{-1} after 500 cycles. Si anode with 120 ppm boron doping (B120) was also prepared, the electrode starts to degrade after 300 cycles and shows a 293 mA h g^{-1} after 500 cycles. Even for surface carbon coated Si anodes, boron doping helps to improve the capacity retention during long-term cycling. To fabricate a Si anode with a high areal capacity of >3 mA h cm^{-2}, the loading of Si/C was further increased up to 2.0 mg cm^{-2} (Fig. 6(b)). At 0.05C, with loadings of 1.5 and 2.0 mg cm^{-2}, the initial specific capacities are 2246 and 1944 mA h g^{-1}, respectively (Fig. S3†), corresponding to areal capacities of 3.4 and 3.9 mA h cm^{-2} (Fig. 6(b)), respectively. The nano-Si shows an initial capacity of 2666 mA h g^{-1} (2.4 mA h cm^{-2}) at 0.05C. After the initial two activated cycles at 0.05C, the specific current was increased to 0.125C. For the nano-Si anode, the capacity faded quickly to 0.72 and 0.43 mA h cm^{-2} after 30 and 80 cycles (Fig. 6(c)), respectively. In contrast, for the B3900 electrode at a loading of 1.5 mg cm^{-2}, the capacity stabilized after the initial 4 cycles and remained at 3.0 mA h cm^{-2} after 80 cycles (Fig. 6(c)). Further increasing the area loading to 2 mg cm^{-2}, the B3900 electrode stabilized after 10 cycles and holds a capacity of 3.2 mA h cm^{-2} until 50 cycles. It is known that a thicker electrode causes larger overpotential, thus lowering the specific capacity. A critical thickness of the Si/C anode should be optimized; herein the thickness for 1.5 mg cm^{-2} is 16 μm. It should be noted that the capacity of B3900 (2.0 mg cm^{-2}) fades seriously after 50 cycles, which may be caused by the electronic contact breakout and the degradation of lithium metal at such a high areal capacity (>3.0 mA h cm^{-2}).[29] The thickness of the B3900 electrode with a loading of 2.0 mg cm^{-2} has been characterized by SEM (Fig. 6(d)), and the pristine thickness is 18 μm, corresponding to
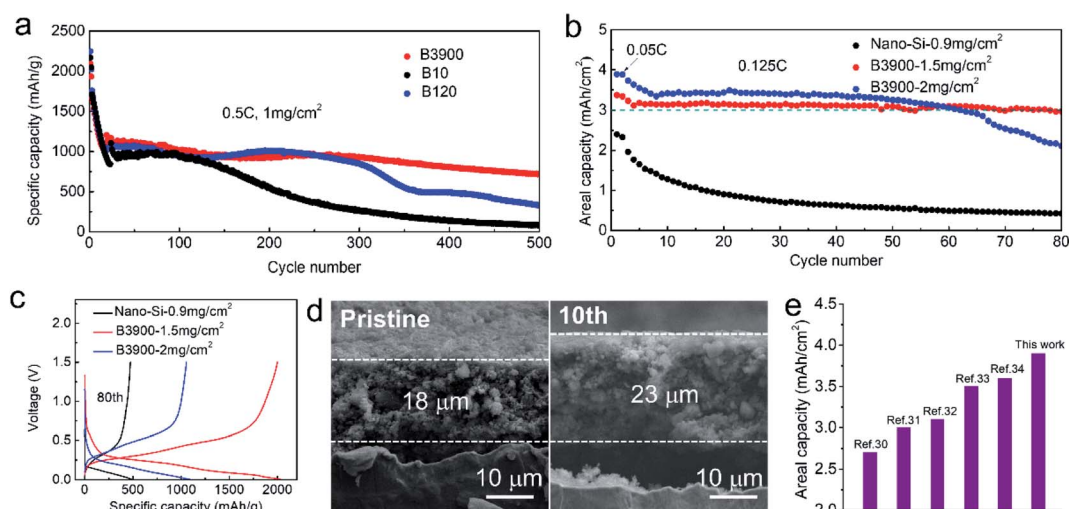

Fig. 6 (a) The cycling performance of carbon coated boron doped Si anodes at 0.5C between 0.005 and 1.5 V with different boron doping amounts 10, 120, and 3900 ppm, and the mass loading is around 1 mg cm^{-2}. (b) The performance comparison of high loading boron doped Si (1.5 and 2 mg cm^{-2}) and nano-Si (0.9 mg cm^{-2}) anodes at 0.125C followed by the initial 2 cycles at 0.05C. (c) The capacity voltage profiles of high loading boron doped Si (1.5 and 2 mg cm^{-2}) and nano-Si (0.9 mg cm^{-2}) anodes. (d) The thickness variation of high loading boron doped Si (2 mg cm^{-2}) before cycling and after 10 cycles. (e) Comparison of areal capacities with recently published studies.

This journal is © The Royal Society of Chemistry 2021

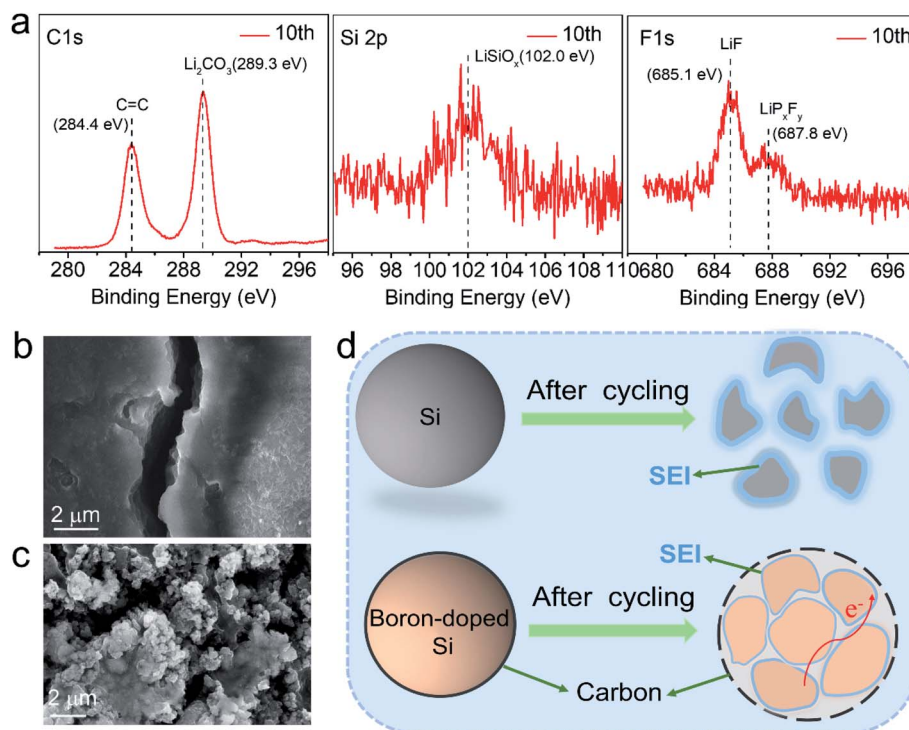*J. Mater. Chem. A*, 2021, **9**, 3628–3636 | **3633**

Fig. 7 (a) The XPS spectra of the carbon coated boron doped Si anode after 10 cycles: C 1s, Si 2p, and F 1s. (b) The surface SEM image of the nano-Si anode after 60 cycles. (c) The surface SEM image of the carbon coated boron doped Si anode after 60 cycles. (d) The schematic mechanism of the fast-charging and stable Si anode enabled by bulk boron doping and surface carbon coating.

2111 mA h cm^{-3}. The thickness increased to 23 μm after 10 cycles, and the volume expansion is about 27%. As shown in Fig. 6(e), our carbon coated boron doped Si anode shows higher areal capacity compared with recent studies published in high impact journals.[30–34]

XPS was carried out to analyse the SEI of carbon coated boron doped Si after 10 cycles (Fig. 7(a)). For C 1s spectra, besides the C=C peak at 284.4 eV,[35,36] a new peak at 289.3 eV was observed, corresponding to the formation of Li$_2$CO$_3$.[35,36] For the Si 2p spectrum, the pristine two peaks converted to a broad peak at 102.0 eV, implying that Li reacted with the surface SiO$_2$ layer and lithium conductive LiSiO$_x$ was formed. For F 1s, a main peak corresponding to LiF (685.1 eV) and a shoulder peak (LiP$_x$F$_y$, 687.8 eV) were detected. With the surface SiO$_2$ layer and carbon coating, the LiSiO$_x$ and LiF in the SEI help to enhance its stability during repeated volume expansion and shrinkage.[37,38] As a result, for the thick B3900 electrode after 60 cycles, separated particles still existed, and only some small cracks are observed while the particles remain integrated (Fig. 7(c)). By contrast, for nano-Si anode, no separate particles observed and the fractured Si immersed into thick SEI (Fig. 7(b)). We summarized the stability mechanism of carbon coated boron doped Si (Fig. 7(d)). The pristine Si expands and cracks into small particles. As a result, the newly exposed Si continuously reacts with the liquid electrolyte and forms a thick SEI, which subsequently blocks lithium ion and electron transportation. By contrast, with surface carbon coating the volume expansion could be accommodated to some extent and the Si particle remains integrated while some cracks are formed

during cycling. Furthermore, due to the high conductivity of boron doped Si, the inter-particle conductivity substantially enhanced, which enables the Si material to be active even when some cracks are formed. The lithium ion transportation and interparticle electrical conductivity play a crucial role in enabling stable cycling performance, especially at a high rate.

Conclusion

In summary, we develop a novel concept that address the issues of the particle fracture and loss of electrical connectivity associated with the large volume change of Si anodes. The strategy is based on surface carbon coating and bulk boron doping. The bulk boron doping enhances the lithium ion transportation in bulk parts and at the interfaces. The boron doping is also demonstrated to improve the interparticle electrical conductivity. As a result, for bare Si film anodes, the rate performance increases, 893 mA h g^{-1} at 8C. With a stabilized solid electrolyte interphase enabled by surface carbon coating, the heavily boron doped Si shows improved capacity retention during a long-term cycling test, above 700 mA h g^{-1} after 500 cycles at 0.5C. Furthermore, an improved mass loading of 2.0 mg cm^{-2}, high areal capacity (3.9 mA h cm^{-2}) and high-volume capacity (2111 mA h cm^{-3}) are achieved. With an optimized mass loading of 1.5 mg cm^{-2}, a high areal capacity of 3.0 mA h cm^{-2} is obtained even after 80 cycles. Our work opens a new horizon for bulk doping and surface coating to engineer Si anodes and such electrodes with large volume changes.

Experimental

Materials synthesis

The deposition of boron doped a-Si was performed on a self-designed radio frequency sputtering system. The targets are single crystalline Si wafers (5–7 mΩ cm and 1–10 Ω cm) with a bonded copper substrate. The boron doping is carried out in the Si wafer preparation process using a diffusion method with B ion injection. The sputtering power is 100 W at 0.8 Pa, and the duration time is 1 h.

The boron doped Si powers were prepared by a ball milling method with polycrystalline boron doped bulk Si (120 mesh) as the starting material. A P type (boron doping) Si material is normally used in the solar cell industry, during the sheet Si fabrication process, and tons of Si waste fragments are formed. The purity of this Si is 99.99%, the boron doping contents (10 ppm, 120 ppm, and 3900 ppm) can be easily controlled during the crystallization and purification processes. The boron-doped polycrystalline Si particles were purchased from Lingyun Silicon Co. Ltd., China. The ball milling process was performed at 600 rpm for 24 hours.

Characterization

Scanning electron microscopy (SEM, Hitachi S4800) was carried out to characterize the surface morphology of the boron doped a-Si film and carbon coated boron doped Si. The interfacial and crystalline structures were characterized by transmission electron microscopy (TEM, Tecnai F30). Powder X-ray diffraction (Rigaku Ultima IV) was used to test the crystalline structure of boron doped Si powders. Raman spectroscopy (WITEC) and Fourier transform infrared spectroscopy (FTIR, Nicolet 380) were applied to identify the chemical structure. X-ray photoelectron spectroscopy (XPS, PHI Quantum 2000) was applied to analyse the interphase covalent bond of the carbon coated boron doped Si before and after cycling. The elemental analysis was carried out using an Elementar: Vario EL cube.

Electrochemical evaluation

To evaluate the electrochemical performance, the boron doped a-Si film on copper foil was directly assembled in a CR2032 cell as the working electrode with Li metal as the counter electrode. For the boron doped Si powders, the powders were firstly mixed with PAN solution at a ratio of 1 : 1 by weight to make a slurry. Then the slurry was cast onto copper foil with a diameter of 14 mm. The electrodes were dried in a vacuum oven at 80 °C for 2 h. Then the PAN coated boron doped Si powder electrodes were transferred into a furnace and heated for 2 h at 700 °C in high purity Ar (99.999%). The mass loading of carbon coated boron doped Si is 1–2 mg cm^{-2}. The carbon coated boron doped Si electrodes were directly assembled into a CR2032 coin cell with lithium metal as the counter electrode. The electrolyte used in all cells was 1 M LiPF$_6$ in ethylene carbonate (EC), dimethylcarbonate (DMC) and diethylcarbonate (DEC) (1 : 1 : 1 vol%) with a 10 wt% fluorinated ethylene carbonate (FEC) additive. The coin cell fabrication was performed in an Ar (99.999%) filled glovebox (Mbraun, H$_2$O, O$_2$ < 0.5 ppm). The

mass loading was weighed with a microbalance (METTLER TOLEDO XS3DU) at an accuracy of 0.001 mg. The galvanostatic cycling was performed using a Land CT2001A system between 0.005 V and 2.5 V at 30 °C. Impedance spectroscopy (VersaSTAT MC, America) was performed from 100 kHz to 10 mHz with an AC amplitude of 20 mV.

Conflicts of interest

The authors declare no conflict of interest.

Acknowledgements

References

1 M. Armand and J. M. Tarascon, *Nature*, 2008, **451**, 652–657.
2 X. Cao, X. Ren, L. Zou, M. H. Engelhard, W. Huang, H. Wang and Y. Cui, *Nat. Energy*, 2019, **4**, 796–805.
3 W. Zhou, J. Chen, M. Chen, A. Wang, A. Huang, X. Xu and C. P. Wong, *J. Mater. Chem. A*, 2020, **8**, 8397–8409.
4 H. Yang, S. Liu, L. Cao, S. Jiang and H. Hou, *J. Mater. Chem. A*, 2018, **6**, 21216–21224.
5 L. Zhao, H. H. Wu, C. Yang, Q. Zhang, G. Zhong, Z. Zheng and T. Zhu, *ACS Nano*, 2018, **12**, 12597–12611.
6 X. Han, H. Chen, J. Liu, H. Liu, P. Wang, K. Huang, C. Li, S. Y. Chen and Y. Yang, *Electrochim. Acta*, 2015, **156**, 11–19.
7 H. Chen, Z. Dong and Y. Fu, *J. Solid State Electrochem.*, 2010, **14**, 1829–1834.
8 Q. Zhang, H. Chen, L. Luo, B. Zhao, H. Luo, X. Han and M. Liu, *Energy Environ. Sci.*, 2018, **11**, 669–681.
9 R. T. Pekarek, A. Affolter, L. L. Baranowski, J. Coyle, T. Hou, E. Sivonxay and C. Apblett, *J. Mater. Chem. A*, 2020, **8**, 7897–7906.
10 J. Chen, X. Fan, Q. Li, H. Yang, M. R. Khoshi, Y. Xu and H. He, *Nat. Energy*, 2020, **5**, 386–397.
11 D. Lee, A. Kondo, S. Lee, S. Myeong, S. Sun, mI. Hwang and U. Paik, *J. Power Sources*, 2020, **457**, 228021.
12 H. Jia, X. Li, J. Song, X. Zhang, L. Luo, Y. He and C. Wang, *Nat. Commun.*, 2020, **11**, 1–9.
13 S. Fan, H. Wang, J. Qian, Y. Cao, H. Yang, X. Ai and F. Zhong, *ACS Appl. Mater. Interfaces*, 2020, **12**, 16411–16416.
14 X. Han, Z. Zhang, H. Chen, R. You, G. Zheng, Q. Zhang and Y. Yang, *J. Power Sources*, 2019, **436**, 226794.
15 J. Shin and E. Cho, *Chem. Mater.*, 2018, **30**, 3233–3243.
16 C. J. Zhang, S. H. Park, A. Seral-Ascaso, S. Barwich, N. McEvoy, C. S. Boland and V. Nicolosi, *Nat. Commun.*, 2019, **10**, 1–9.
17 Y. He, X. Yu, Y. Wang, H. Li and X. Huang, *Adv. Mater.*, 2011, **23**, 4938–4941.

18 Z. Wang, Y. Li, S. Huang, L. Liu, Y. Wang, J. Jim, D. Kong, L. Zhang and O. G. Schmidt, *J. Mater. Chem. A*, 2020, **8**, 4836–4843.

19 R. Fang, W. Xiao, C. Miao, P. Mei, Y. Zhang, X. Yan and Y. Jiang, *Electrochim. Acta*, 2019, **317**, 575–582.

20 Y. Domi, H. Usui, M. Shimizu, Y. Kakimoto and H. Sakaguchi, *ACS Appl. Mater. Interfaces*, 2016, **8**, 7125–7132.

21 M. Chen, Q. Zhou, J. Zai, A. Iqbal, T. Tsega, B. Dong, X. Liu and Y. Zhang, *Nano Res.*, 2021, **14**, 1004–1011.

22 J. Ryu, J. Seo, G. Song, K. Choi, D. Hong, C. Wang, H. Lee, J. Lee and S. Park, *Nat. Commun.*, 2019, **10**, 2351.

23 M. Chen, B. Li, X. Liu, L. Zhou, L. Yao, J. Zai, X. Qian and X. Yu, *J. Mater. Chem. A*, 2018, **6**, 3022–3027.

24 S. Cangaz, F. Hippauf, F. S. Reuter, S. Doerfler, T. Abendroth, H. Althues and S. Kaskel, *Adv. Energy Mater.*, 2020, **10**, 2001320.

25 M. J. Kang, M. Kim, E. S. Hwang, J. Noh, S. T. Shin and B. H. Cheong, *J. Soc. Inf. Disp.*, 2019, **27**, 34–40.

26 X. Han, H. Chen, X. Li, J. Wang, C. Li, S. Chen and Y. Yang, *J. Mater. Chem. A*, 2016, **4**, 434–442.

27 Y. Tang, Y. Zhang, W. Li, B. Ma and X. Chen, *Chem. Soc. Rev.*, 2015, **44**, 5926–5940.

28 N. Ding, J. Xu, Y. X. Yao, G. Wegner, X. Fang, C. Chen and I. Lieberwirth, *Solid State Ionics*, 2009, **180**, 222–225.

29 X. Li, J. Zheng, X. Ren, M. H. Engelhard, W. Zhao, Q. Li and W. Xu, *Adv. Energy Mater.*, 2018, **8**, 1703022.

30 H. J. Kwon, J. Y. Hwang and H. J. Shin, *Nano Lett.*, 2019, **20**, 625–635.

31 H. Jia, X. Li and J. Song, *Nat. Commun.*, 2020, **11**, 1–9.

32 J. Wang, L. Liao and H. R. Lee, *Nano Energy*, 2019, **61**, 404–410.

33 Y. An, Y. Tian and H. Wei, *Adv. Funct. Mater.*, 2020, **30**, 1908721.

34 Y. Son, N. Kim and T. Lee, *Adv. Mater.*, 2020, **32**, 2003286.

35 S. Bhattacharya, A. R. Riahi and A. T. Alpas, *Carbon*, 2014, **77**, 99–112.

36 P. Guan, L. Liu and X. Lin, *J. Electrochem. Soc.*, 2015, **162**, A1798.

37 X. Han, Z. Zhang and H. Chen, *J. Power Sources*, 2019, **436**, 226794.

38 J. Wang and Y. Cui, *Nat. Energy*, 2020, **5**, 361–362.

3636 | *J. Mater. Chem. A*, 2021, **9**, 3628–3636

This journal is © The Royal Society of Chemistry 2021